scientific reports

Check for updates

OPEN

Unveiling the mechanism secret of abrasion emissions of particulate matter and microplastics

Ketian Li, Kunhao Yu, Yanchu Zhang, Haixu Du, Constantinos Sioutas✉ & Qiming Wang✉

Recent research highlights that non-exhaust emissions from the abrasion of tires and other organic materials have emerged as a substantial source of airborne particulate matter and marine microplastics. Despite their growing impact, the underlying mechanisms driving these abrasion emissions have remained largely unexplored. In this study, we uncover that abrasion emissions from organic materials are fundamentally governed by a fatigue fracture process, wherein particles are progressively detached from the material surface under cyclic abrasion loads. Our findings demonstrate that these emissions increase significantly only when the applied abrasion loads surpass the material's toughness threshold. We establish a scaling relationship between the concentration of emitted particulate matter and the measurable crack propagation rate of the organic material, offering a robust quantitative method to estimate abrasion emissions. This work not only introduces a novel mechanistic framework for understanding particulate matter pollution from organic material abrasion but also provides a scientific basis for developing strategies to mitigate emissions of airborne particulates and marine microplastics.

Keywords Particulate matter, Marine microplastics, Abrasion emission, Tire emission, Fatigue fracture

When an organic material undergoes cyclic friction with an engineering object with a higher hardness, the organic material will be abraded to emit particulate matter (PM). Such an abrasion emission phenomenon can be widely observed in daily life examples, such as tire particle emissions from automobiles (Fig. 1A), organic brake pad particle emissions from vehicles or engines (Fig. 1B), and shoe sole particle emissions from footwear (Fig. 1C). As direct tailpipe emissions of particulate matter have been significantly reduced by tight government regulations and the adoption of electric vehicles has been drastically increasing, non-exhaust emissions, such as tire and brake emissions, have become a major source of airborne particulate matter in the urban areas[1–5]. According to a report from the United Kingdom Government's Air Quality Expert Group in 2019[6], non-exhaust emissions constitute 60% PM2.5 and 73% PM10 from road transport. In addition, researchers have revealed that particles released from vehicle tires are previously unrecorded but indeed significant sources of microplastics in the marine environment[7–10]. For example, it has been estimated that about 100,000 metric tons of microplastics are shed from tires, transported through the air, and dumped in the ocean every year[11].

Worse still, a great proportion of particles emitted from abrasion emissions are microplastic particles, tiny plastic pieces less than 5 mm long, which are challenging to naturally degrade in the environment and tend to accumulate over time[12–14]. Larger particles could gradually break down into smaller particles that can potentially be inhaled by humans[15–21]. Since airborne particulate matter poses a high health risk to humans[22–25] and marine microplastics detrimentally affect the marine ecological metabolism[7–10], modern society is urgently calling for effective strategies for mitigating their emissions from the abrasion of tires and other organic materials. However, without understanding the fundamental mechanisms of the abrasion emission, any ill-informed strategies may become ineffective.

To uncover the mechanism secret of abrasion emissions from tires and other organic materials, previous studies are primarily focused on the experimental characterization of abrasion emissions of particulate matter in the lab[26,27] or the field[3,28]. Despite the enormous effort, the fundamental mechanism of abrasion emissions of organic materials has remained largely elusive to date[1,2,29]. Some researchers believe abrasion should be a mechanics problem that is associated with material fracture[30–36], while others believe abrasion emissions may be associated with thermally induced burning of organic materials[1,2]. Even for those who consider abrasion emission as a fracture mechanics problem[30–36], a mechanistic understanding of the relationship between abrasion emissions and the mechanical properties of organic materials remains unknown. A mechanistic understanding

Sonny Astani Department of Civil and Environmental Engineering, University of Southern California, Los Angeles, CA 90089, USA. ✉email: sioutas@usc.edu; qimingw@usc.edu

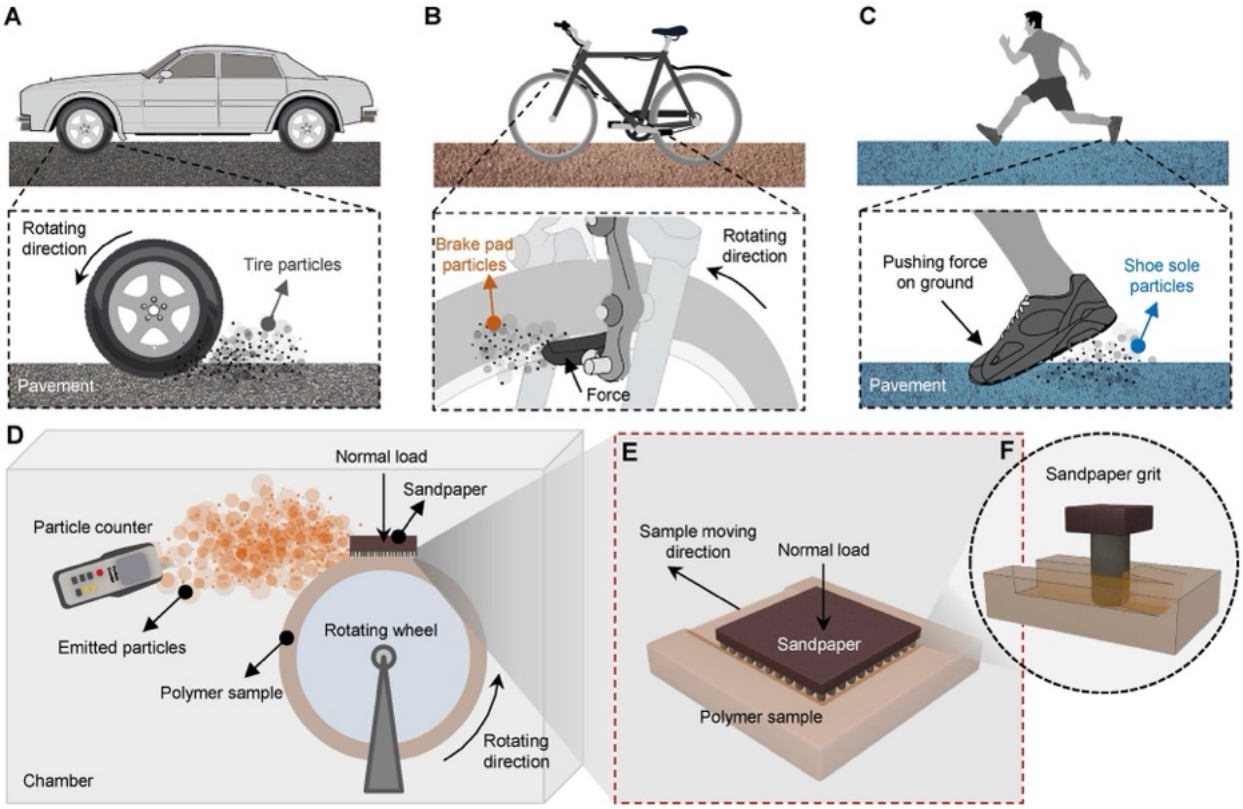

Fig. 1. Daily-life abrasion emission examples and the proposed setup for abrasion emission experiments. (**A**) Tire particle emissions from an automobile. (**B**) Organic brake pad particle emissions from a bicycle. (**C**) Shoe sole particle emissions from footwear. (**D**) The proposed setup for abrasion emission experiments. A motor-controlled rotating wheel with a polymer sample firmly attached to the wheel is housed in a closed chamber. Sandpaper is forced to abrade the moving polymer sample to emit particles that are detected by a particle counter. (**E**) A zoom-in schematic to illustrate the contact between the sandpaper and the polymer sample. (**F**) A further zoom-in schematic to illustrate the abrasion fracture induced by a sandpaper grit.

framework, if successfully established, would provide rational and quantitative guidance for mitigating abrasion emissions of airborne particulate matter[1–3] and marine microplastics[7–10].

Here, we uncover the secret of abrasion emissions by establishing a mechanistic linkage between the abrasion emissions of organic materials and their mechanical properties. We hypothesize that the abrasion emission is a *fatigue fracture process* that organic particles are abraded and detached from the material bulk under cyclic abrasion loading. Thus, the emission of the particulate matter is closely related to the effective energy release rate applied by the cyclic abrasion loading[30–36]. We discover that abrasion emissions start to drastically increase only when the abrasion-induced effective energy release rate exceeds the fatigue toughness threshold of the organic material. Above the fatigue toughness threshold, the surface area density of the emitted particulate matter scales with the crack propagation area rate of the fatigue fracture. These discoveries have been experimentally verified with synthetic polyurethane polymers that feature various crystallinities and are loaded with kinetic frictions with various normal loads and surface roughnesses. We also verify the discoveries with various abrasion emission sources in daily life: tires from automobiles, brake pads from bicycles, and rubber soles from footwear. The discoveries in this report verify a mechanics mechanism and also derive rational guidance for mitigating the abrasion emissions of airborne particulate matter and marine microplastics.

Experimental setting and mechanism hypotheses

To mimic the abrasion emission induced by cyclic friction in daily life (Fig. 1A–C), we constructed an experimental system as shown in Fig. 1D and S1. A motor-controlled rotating wheel with a polymer sample firmly attached to the wheel was housed in a closed chamber. Sandpaper was forced to contact the polymer sample with a prescribed normal force that was controlled by a force gauge. When the motor was turned on, the polymer particles were emitted from the abrasion between the polymer sample and the sandpaper. A particle counter (TENMA, 72-10190) placed at 20 cm to the abrasion location was used to measure the concentration of the emitted particles with sizes ranging from 0.3 to 10 μm. We choose particles below 10 μm (PM10) for the measurement because PM10 is the size range of primary airborne particulate matter harmful to human health[1–3].

To understand the abrasion emission in the experimental setting shown in Fig. 1D, we here propose a mechanics hypothesis. Similar to the tire abrasion of a moving automobile (Fig. 1A), the polymer sample is abraded cyclically by the sandpaper. Considering the nature of cyclic loading, we hypothesize that the emission

of the polymer particles is due to a fatigue fracture process[37–39], in that polymer materials are fractured and detached from the material bulk under cyclic abrasion loading. During the abrasion loading, sandpaper with N_g grits (each grit with a circular cross-section with a mean diameter of ρ) is forced by a normal load F_N to indent into the polymer sample by a depth of d (Fig. 1E,F). The indentation depth d of each grit can be estimated as $d \approx F_N(1-\nu^2)/(2\rho E N_g)$, where E and ν are Young's modulus and Poisson's ratio of the polymer sample, respectively[40]. As the polymer sample is moving with the rotating wheel, the sandpaper abrades the polymer by using a friction force F_T to fracture and detach the polymer materials in front of the sandpaper grits (Fig. 1F). During this process, There are two main processes that take place simultaneously. On the macro level, the original materials would form a macroscopic crack on the scratched surface as the hard object cuts and scoops the original material. The macrocrack are the primary cause of material detachment. Meanwhile, the original material will generate numerous microcracks within the matrix. These microcracks will also continue to propagate under cyclic loads and become the reason for the material to split into smaller particles after detaching from the matrix. The applied enegegy release rate of the macrocrack could be a dominant factor for the abrasion emissions. Such an abrasion mechanics problem has been solved by Akono et al.[33,34] who approximated the applied energy release rate as $G_a = F_T^2\left(1-\nu^2\right)/\left[2E\rho^2N_g^2d\left(1+2d/\rho\right)\right]$, where the friction force $F_T = \mu F_N$ and μ is the kinetic friction coefficient that is affected by the surface roughness. Substituting the indentation depth d into G_a, we can estimate the applied energy release rate to fracture and abrade the polymer as

$$G_a = \frac{\mu^2 F_N \rho E}{\rho^2 E N_g^2 + F_N(1-\nu^2)}. \tag{1}$$

According to the theory of fatigue fracture proposed by Paris et al.[37] and the later studies that applied the fatigue fracture theory to rubbers[38,39], when a cyclic load is applied to a solid with a pre-existing crack, there is a material property called *fatigue fracture toughness threshold* G_c that determines whether the fatigue crack will propagate or not. Based on this concept, we propose the following mechanics hypothesis: When $G_a < G_c$, the pre-existing crack is expected not to propagate under infinite cycles of loads, which means that the polymer materials will ideally not be abraded and detached from the material bulk, thus corresponding to a very low concentration of abrasion emissions of particulate matter. However, when $G_a > G_c$, the pre-existing crack is expected to propagate under cyclic loads, leading to a relatively high concentration of abrasion emissions of particulate matter, which should be quantitatively relevant to the crack propagation rate of the fatigue fracture under the applied loads.

Hypothesis validation with polyurethanes of various fatigue toughnesses

To validate the above mechanism hypothesis, we select a class of polyurethanes as a model material system, because the fatigue fracture toughness of polyurethane rubbers can be widely tuned by simply varying the polymer chain length (Fig. S2)[41]. The polyurethanes with shorter chain lengths feature higher crystallinities that are expected to result in higher fatigue fracture toughness (Fig. S2), because the energy per unit area required to fracture crystalline domains in a polymer is much higher than that required to fracture the amorphous domain[42,43]. Here we denote these polyurethane samples as PU-A to PU-E for crystallinities of 53.3, 42.7, 29.8, 20.6, and 9.9, respectively (Fig. S2). To measure the fatigue property of polyurethanes, we employ the single-notched method that has been widely used in fatigue tests of polymer materials (Fig. S3) (see Material and methods section: "Measurement of fatigue properties")[38,39]. Specifically, we use an unnotched sample under a cyclic stretch λ^A (with a frequency of 5 Hz) to estimate the energy release rate G and use a single-notched sample under the same cyclic stretch λ^A to observe the crack propagation per loading cycle dc/dN, namely, crack propagation area rate, where c is the crack surface area (i.e. crack length times sample thickness) and N is the cycle number. For each material shown in Fig. 2A, the crack propagation area rate dc/dN first remains to be close to zero with increasing energy release rate at the beginning, and starts to increase only after the applied energy release rate is above the fatigue toughness threshold G_c. The fatigue toughness threshold G_c indicates a critical point where the crack begins to propagate under the applied cyclic load. As expected, G_c increases with increasing crystallinity within the polyurethane (Figs. 2A and S4).

Using the testing chamber shown in Fig. 1D, we carry out the particulate matter emission tests for polyurethane samples for 2 min (the same rotating frequency of 5 Hz and the same normal force of 3 N, "Materials and methods"). For each polyurethane sample, the measured particle concentration n (in particle number/L) decreases with increasing particle sizes d from 0.3 to 10 μm (Fig. 2B). Compared among polyurethane samples, the overall concentrations (i.e. $\sum n$) of the emitted PM10 increase as the fracture toughness of polyurethanes decreases (Fig. S5). This means that it becomes more difficult to emit PM10 particles for tougher polyurethane. This finding can be indirectly verified by imaging contaminated glass slides (initially clean) within the experimental chamber (Fig. S6). The microscopic images of these glass slides show that fewer particles are attached to the slides if the toughness of the polyurethane is higher (Fig. S6B). In addition, we find that though the concentrations of emitted PM10 decrease with increasing fatigue threshold G_c, such a decreasing relationship (i.e., $\sum n$ versus G_c) does not follow a linear relationship (Fig. S5).

To obtain a deterministic scaling law for the PM emissions, we apply one experimental condition (i.e. the same normal load $F_N = 3$ N, the same sandpaper, and the same wheel rotation frequency of 5 Hz) to five types of polyurethane samples. Under this experimental condition, the applied energy release rate G_a (Eq. 1) for PU-A is below the fatigue threshold G_c (Fig. 2C); while G_a for others (PU-B to PU-E) are all above the corresponding fatigue threshold G_c (e.g. PU-E shown in Fig. 2D). We find that the PM10 concentration emitted from PU-A is drastically lower than those from the other four polyurethane samples (Fig. 2E). For example, the PM10 concentration emitted from PU-A is only 29.5% of that from PU-B, 27.5% of that from PU-C, 26% of that from PU-D, and 15.8% of that from PU-E. Such an ultra-low PM10 concentration can be attributed to the close-to-

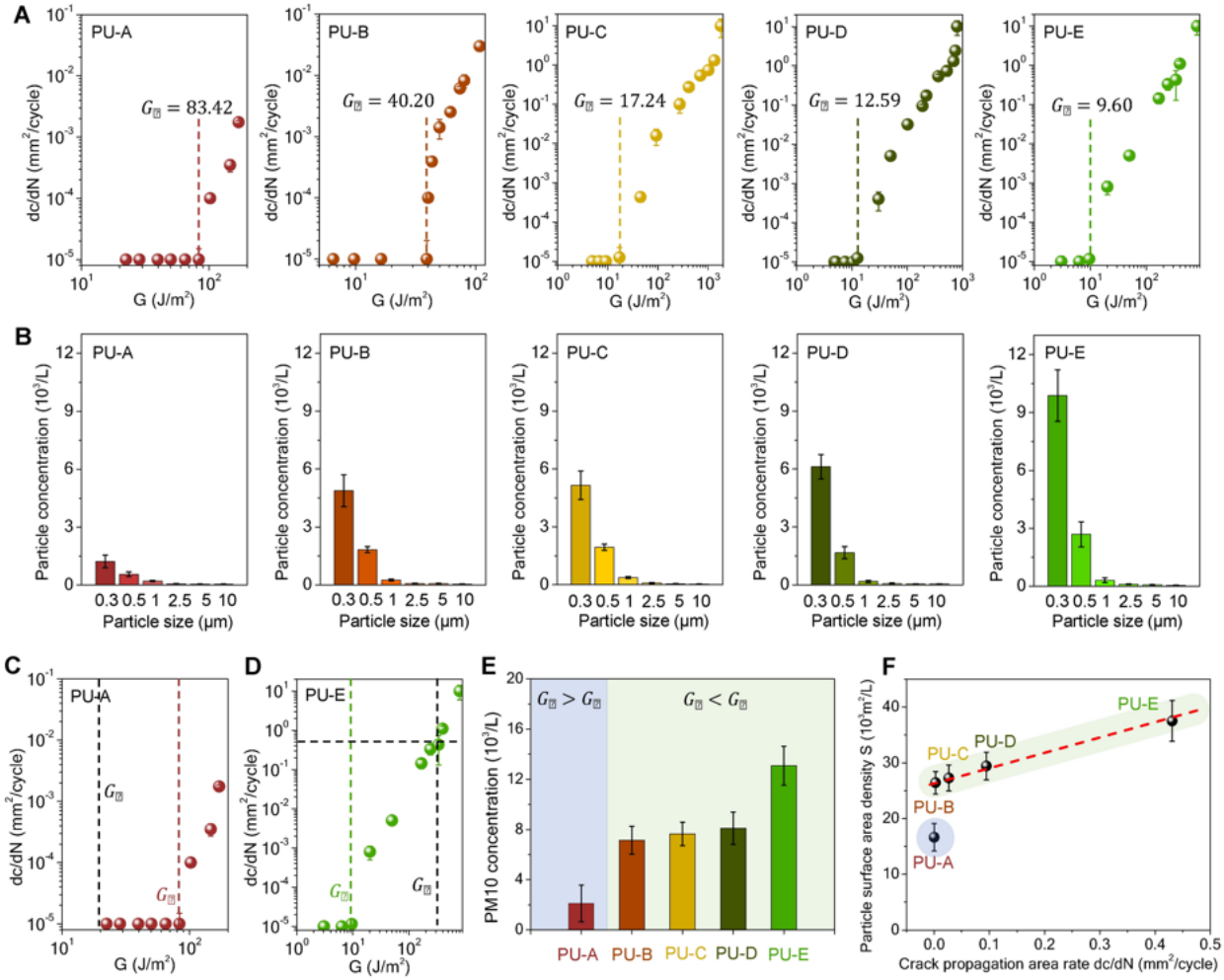

Fig. 2. Mechanistically relating the abrasion emission of polyurethanes to their fatigue fracture properties. (1) Fatigue properties of 5 types of polyurethane samples (PU-A to PU-E): the crack propagation area rates dc/dN for cyclic loads in functions of the corresponding energy release rate G. The dashed lines indicate the fatigue toughness threshold G_c. (**B**) The concentrations of emitted particles with size from 0.3 μm to 10 μm for polyurethane samples PU-A to PU-E. (**C**) Crack propagation area rates dc/dN in a function of energy release rates G for PU-A. The applied energy release rate G_a is smaller than the fatigue toughness threshold G_c of PU-A. (**D**) Crack propagation area rates dc/dN in a function of energy release rates G for PU-E. The applied energy release rate G_a is larger than the fatigue toughness threshold G_c of PU-E. (**E**) PM10 concentrations of polyurethane samples PU-A to PU-E under the same applied energy release rate G_a. Two shaded areas indicate two regions corresponding to $G_c > G_a$ and $G_c < G_a$, respectively. (**F**) Particle surface area densities S in a function of crack propagation area rates dc/dN for polyurethane samples PU-A to PU-E. Error bars in (**A**), (**C**) and (**D**) represent standard deviations of 3 samples. Error bars in B, E, and F represent standard deviations of 5–10 tests.

zero crack propagation rate when the applied cyclic load only provides a very small energy release rate, i.e., $G_a < G_c$ (Fig. 2C).

When the crack propagation rate is non-zero (i.e. $G_a > G_c$), we assume that cracks are required to propagate approximately through half the surface area of a particle to be able to fully detach the material to become an isolated particle. Then, the total crack propagation area should scale with the half particle surface area density (per unit volume), i.e. $\sum \left(n\pi {D_P}^2/2\right)$, where D_P is the particle diameter. Besides, the total crack propagation area should scale with $(dc/dN)\, N_{total}$, where N_{total} is the total loading cycle number. Since we employ the same total loading cycle number N_{total} (with a fixed loading time and frequency), we can write a scaling law between the total particle surface area density (per unit volume) S and the crack propagation area rate as

$$S = \sum \left(n\pi {D_p}^2\right) \propto \frac{dc}{dN}. \tag{2}$$

To estimate dc/dN for each material, we need to first calculate the applied energy release rate G_a from Eq. (1) and then harness the dc/dN versus G relationship (see black dash lines in Fig. 2D) to estimate the corresponding

dc/dN. As shown in Fig. 2F, for those materials with $G_a > G_c$ (PU-B to PU-E), S displays a clear linear relationship with the corresponding dc/dN, illustrated by the red dashed line. However, for PU-A with $G_a < G_c$, the data point is below the red dashed line; this is because the crack is not supposed to propagate when the applied energy release rate is below the fatigue toughness threshold. Based on the experimental results from Fig. 2F, we reach a tentative conclusion: the abrasion emission rate begins to drastically increase only when the abrasion-induced energy release rate exceeds the fatigue toughness threshold; above the fatigue toughness threshold, the surface area density of the emitted PM10 is linearly proportional to the crack propagation area rate.

Verification with polyurethanes under various loading conditions

To verify the above tentative conclusion, we carry out abrasion emission experiments with the same polyurethane (PU-B) under various loading conditions (Fig. 3). First, since the normal force is a significant factor affecting the abrasion process, we examine the effect of the normal force on the abrasion emission (Fig. 3A,B). As shown in Fig. 3A, the measured PM10 concentration does not follow a simple linear relationship with the applied normal force, but apparently falls into two groups: When the normal force is below a threshold, the PM10 concentration remains relatively small and is almost independent of the applied normal force; once the normal force is above the threshold, the PM10 concentration drastically bumps up and then increases with increasing normal forces. After converting the normal force to the applied energy release rate using Eq. (1), we find that such a threshold is corresponding to the fatigue toughness threshold G_c (i.e. 40.2 J/m^2): Only when $G_a > G_c$, the PM10 concentration starts to drastically increase (Fig. 3A). As shown in Fig. 3B, the particle surface area densities S for different normal forces are plotted in a function of the corresponding estimated crack propagation area rates dc/dN. When $G_a > G_c$, S displays a linear relationship with dc/dN, indicated by a red dashed line, while those S for lower normal forces sit far below the red dashed line.

Next, since surface roughness is another important factor affecting the abrasion emission, we carry out the PM emission experiments using different types of sandpaper with varied surface roughness (Fig. 3C,D). We select 7 types of sandpaper and analyze their grit size distributions using a scanning electron microscope (Fig. S7). The mean diameters of the sandpaper grits ρ vary from 62 to 380 μm. With experimental measurements (see "Materials and methods" section: "Measurement of the coefficient of friction of the sandpapers"), we find that the kinetic friction coefficients μ increase with increasing mean diameters of the sandpaper grits ρ (Fig.

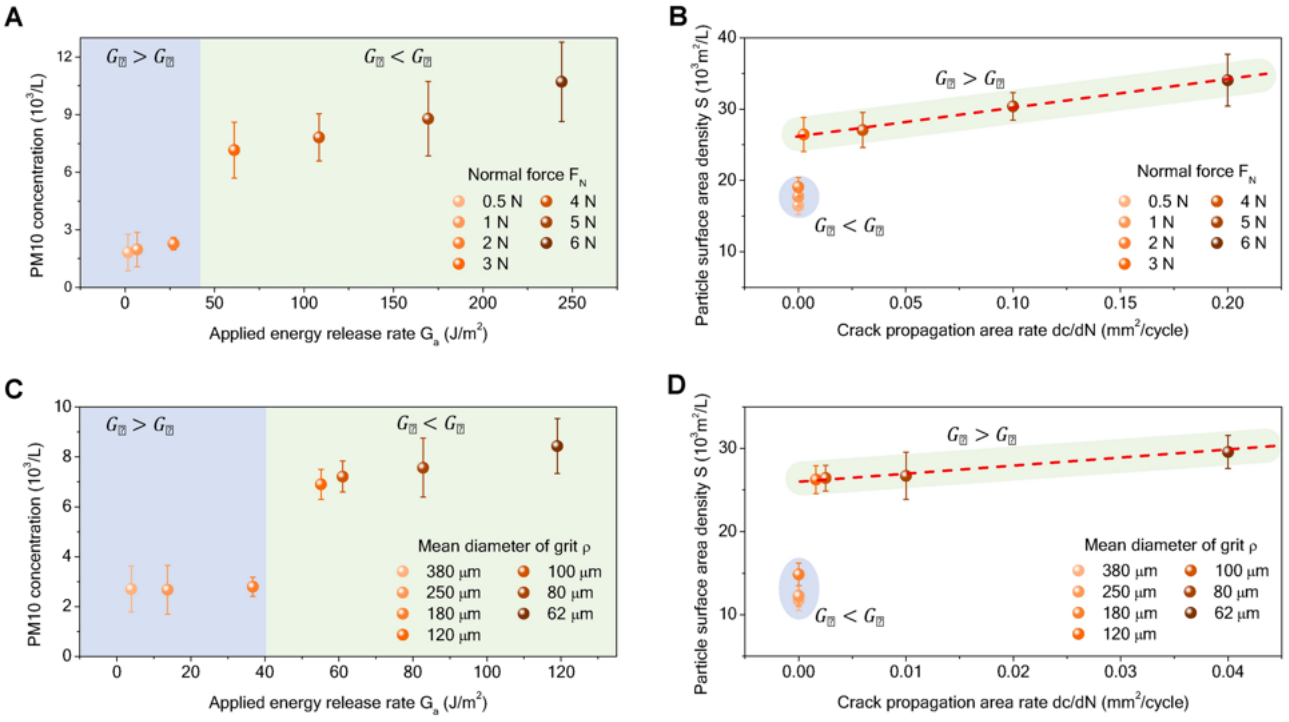

Fig. 3. Mechanism verification with polyurethanes under various loading conditions. (**A**) PM10 concentrations of polyurethane samples PU-B in a function of the applied energy release rates G_a induced by varied normal forces F_N. Two shaded areas indicate two regions corresponding to $G_c > G_a$ and $G_c < G_a$, respectively. (**B**) Particle surface area densities S in a function of crack propagation area rates dc/dN for polyurethane samples PU-B under varied normal forces F_N. (**C**) PM10 concentrations of polyurethane samples PU-B loaded by sandpaper with grits of different sizes in a function of the applied energy release rates G_a. (**D**) Particle surface area densities S in a function of crack propagation area rates dc/dN for polyurethane samples PU-B loaded by sandpaper with grits of different sizes. Error bars in (**A**–**D**) represent standard deviations of 5–10 tests.

S7C). According to Eq. (1), the applied energy release rates increase with decreasing grit sizes ρ (horizontal axis of Fig. 3C). Then, we plot the PM10 concentration as a function of the applied energy release rates for various grit sizes ρ (Fig. 3C). As expected, the PM10 concentration remains relatively low when $G_a < G_c$ and increases abruptly when $G_a > G_c$. Besides, the particle surface area densities S show a linear scaling with the crack propagation area rate dc/dN only for the cases with $G_a > G_c$ (Fig. 3D).

Verification with source materials for daily-life abrasion emissions

To further verify the generalization of the proposed mechanism for abrasion emissions, we next carry out experiments with representative source materials for daily-life abrasion emissions. For example, we obtain the source materials for automobile tires (Fig. 4A), bicycle brake pads (Fig. 4B), and shoe soles (Fig. 4C). Fatigue tests are employed by using cyclic loads of 5 Hz to determine the relationships between the energy release rate G and the crack propagation area rate dc/dN (Fig. 4A–C). The fatigue toughness thresholds G_c can be determined from the dc/dN versus G relationships. Next, we use the source materials to carry out the abrasion emission experiments to measure the emitted PM10 concentrations under sandpaper frictions with an angular frequency of 5 Hz (Fig. 4D–F). The experimental results of the abrasion emissions provide further corroboration of the proposed mechanism: For each source material, when the normal force is large enough to enable the applied energy release rate $G_a > G_c$, the particle surface area densities S linearly scale with the corresponding crack propagation area rates dc/dN, indicated by the red dashed lines (Fig. 4D–F). However, when $G_a > G_c$, the particle surface area densities S are well below the red dashed lines.

Guidance for mitigating abrasion emissions

The results from this report clearly derive two strategic recommendations for mitigating the abrasion emissions of airborne particulate matter and marine microplastics. First, it is recommended that fatigue toughness thresholds of organic materials that are frequently used in abrasion settings, such as tires, brake pads, and shoe soles, should be designed to be well above the applied energy release rates in the possible loading settings. Taking vehicle tires as an example, for a vehicle with a certain weight W_T, having tour tires. The kinetic friction coefficient between the tire and the road is f_T. The roughness of the road is R_a, meaning average, or arithmetic average of profile height deviations from the mean line. From the definition, it can be understood that the road surface roughness R_a can be analogously compared to the size of the grit on sandpaper. Substituting $F_N = W_T g/4$ and $\rho = R_a$ into the Eq. (1), the applied energy release rate G_a can be roughly estimated as Eq. (3).

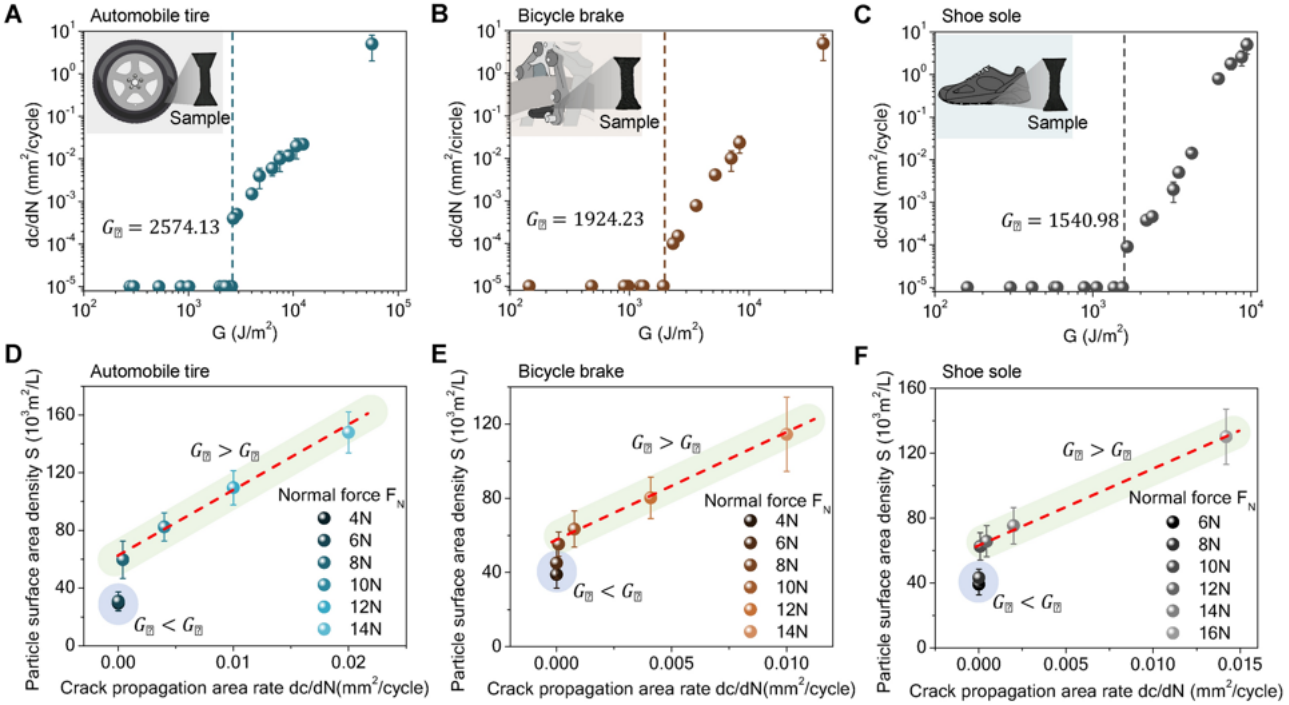

Fig. 4. Mechanism verification with source materials for daily-life abrasion emissions. (**A**–**C**) Fatigue properties of an automobile tire (**A**), a bicycle brake (**B**), and a shoe sole (**C**): the crack propagation area rates dc/dN for cyclic loads in functions of the corresponding energy release rate G. The dashed lines indicate the fatigue toughness threshold G_c. (**D**–**F**) Particle surface area densities S in functions of crack propagation area rates dc/dN for organic samples from an automobile tire (**D**), a bicycle brake (**E**), and a shoe sole (**F**). Error bars in (**A**–**C**) represent standard deviations of 3 samples. Error bars in (**D**–**F**) represent standard deviations of 5–10 tests.

$$G_a = \frac{{f_T}^2 W_T g R_a E}{4{R_a}^2 E N_g^2 + W_T g(1-\nu^2)}. \quad (3)$$

The tire material should be designed to feature a fatigue toughness threshold G_c well above G_a, for example, $G_c = \phi G_a$, where ϕ is a safety factor with a typical value of 3–5. Note that heavier vehicles should use tire materials with higher fatigue toughness thresholds G_c. Regulations should be established to forbid the usage of commercial tires with $G_c \leq G_a$ for different vehicle weights. The industrial standards for selecting tire materials for vehicles with different weights should be significantly reformed to involve the consideration of the impact of the fatigue toughness property on the abrasion emissions.

Second, it is recommended that state and federal authorities should establish annual abrasion emission tests for the organic materials that are frequently used in abrasion settings. This is because the fatigue toughness of organic materials would degrade over long-term service time[44], and the abrasion emission may drastically increase if the material is degraded. Taking vehicle tires as an example, during the abrasion emission tests, varied weight loadings within the normal service weight range should be applied to the vehicle to measure the concentration of the emitted particulate matter (i.e. PM10) around the tires. If the PM10 concentration does not vary substantially over various weight loading, the vehicle tires should be considered to be in a good condition. However, if the PM10 concentration evidently increases with increasing weight loadings, the applied energy release rate may already exceed the fatigue toughness, and therefore, the vehicle tires should be replaced.

In summary, we hypothesize the abrasion emission of organic materials as a fatigue fracture process and validate the hypothesis with various organic materials under various cyclic loading conditions. We demonstrate that the fatigue toughness threshold of the organic material governs the onset of abrasion emissions, and that after onset, the concentration of the emitted particulate matter can be estimated based on the crack propagation area rate of the fatigue fracture. We expect that our discoveries may fundamentally reform strategies that governmental agencies may take to mitigate abrasion emissions, for example, by reforming industrial standards for selecting tire materials and installing abrasion emission tests for vehicle tires to ensure low abrasion emissions. The results of this report dismiss the previously-believed thermal-burning hypothesis[1,2] but verify a mechanism of fatigue fracture mechanics. The mechanism framework of this work opens new and promising venues for understanding abrasion emissions of particulate matter and microplastics by constructing the linkage between fracture mechanics and air pollution.

Due to the more severe adverse effects of particles with diameters less than 0.3 μm on human health, there is significant research potential in developing more accurate measurement and predictive methods for particles below 0.3 μm . However, limited by the employed measurement instrument, this paper only focuses on particles between 0.3 μm and 10 μm. The emission of particles below 0.3 μm is not discussed in this paper but demands careful study in the future. Additionally, effects of long-term and environmental accumulation on the abrasion emission should also be considered in future studies.

Materials and methods

Materials

Poly(tetrahydrofuran) (PolyTHF, average Mn ~ 250, 650, 1000, 2000 g/mol), isophorone diisocyanate (IPDI), Ethyl acetate, dibutyltin dilaurate (DBTDL). All chemicals were purchased from Sigma-Aldrich, USA, and were used without further purification. The automobile tires were obtained from the Continental company. The size is 215/55R18. Section Width is 215 Millimeters. Season is non-winter. Load Index is 94.0. Load Capacity is 2000 Pounds. The shoe sole (Brand: MIIDII) was purchased from Amazon. Product Dimensions is 12.5 × 5 × 0.15 inches with 11.99 Ounces. Bicycle brake (Brand: Lomodo) was purchased from Amazon. Size of rubber pad is 1.57 inch/4 cm in length, 0.55 inch/1.4 cm in height, 0.4 inch/1 cm in thickness, the total height is 0.866 inch/2.2 cm. Bike Type is Mountain Bike, Road Bike Mountain, BMX Bike.

Preparation of polyurethane samples

To prepare the polyurethane samples, we first preheated a total of 0.025 mol of PolyTHF with various molecular weights (for Material A: 0.025 mol of PolyTHF (Mn ~ 250); for Material B: 0.015 mol of PolyTHF (Mn ~ 250) and 0.01 mol of PolyTHF (Mn ~ 650); for Material C: 0.015 mol of PolyTHF (Mn ~ 250) and 0.01 mol of PolyTHF (Mn ~ 1000); for Material D: 0.015 mol of PolyTHF (Mn ~ 650) and 0.01 mol of PolyTHF (Mn ~ 1000); for Material E: 0.015 mol of PolyTHF (Mn ~ 250) and 0.01 mol of PolyTHF (Mn ~ 2000) at 90 °C and bubbled with nitrogen for 1 h to remove water and oxygen. After being cooled to room temperature, 200 wt.% of Ethyl acetate was mixed with the PolyTHF with magnetic stirring for 1 h. 0.025 mol of IPDI was then added to the mixture with magnetic stirring for another 1 h. To complete the synthesis, 2 wt.% of DBTDL was added to the mixture with magnetic stirring for 24 h. During the synthesis process, nitrogen was continuously bubbled in the solution to prevent a reaction between the mixture and the oxygen. After the synthesis process, the obtained solution was poured into a glass mold and placed into a vacuum chamber for 72 h to evaporate the solvent.

Measurement of polyurethane crystallinities

The crystallinities of polyurethane samples were measured by differential scanning calorimetry (DSC/cell: RCS1-3277, cooling system: DSC1-0107). For each material, the sample was cut into pieces and weighed as m_{sample}. The sample was placed into the DSC and heated up from 50 to 200 °C at the rate of 20 °C/min. During the process, the sample was under a nitrogen atmosphere with a flow rate of 30 mL/min. There is an endothermic transition ranging from 120 °C to 160 °C in the curve of heat flow, indicating the melting of the crystalline domains. The fusion enthalpy for the crystalline domains $H_{crystalline}$ can be calculated by integrating the narrow peak ranging

from 120 to 160 °C. Therefore, the crystallinities can be calculated as $X = H_{crystalline}/(m_{sample} \cdot H^0_{crystalline})$ where $H^0_{crystalline} = 167\mathrm{J/g}$ is the fusion enthalpy of 100 wt.% crystalline measured at the equilibrium melting point[45,46].

Measurement of Young's modulus E and Poisson's ratio ν

The Dynamic mechanical analyzer (DMA 850, TA instrument) was used to measure the Young's modulus E of materials at 5 Hz and the amplitude was set as 5 μm. The Poisson's ratio ν was obtained by measuring the lateral strain upon an axial compression.

Measurement of fatigue properties

To measure the fatigue properties of the prepared materials, the single-notch method was adopted[43]. The notched and unnotched dog-bone shaped samples were prepared with 5 mm in width, 10 mm in length, and 1 mm in thickness in their testing region. The notched sample was given a 1 mm initial crack on the edge by a sharp blade (Fig. S3A). The Dynamic mechanical analyzer (DMA850, TA instrument) was used to conduct cyclic tensile tests on the samples. For all the samples, the frequency was set as 5 Hz. In each experiment, we choose a maximum applied stretch λ_{max} and conducted cyclic tensile tests on unnotched samples. The curves of nominal stress P versus stretch λ of the unnotched samples were obtained. After several cycles, the curves of P versus λ in the process of loading and unloading tend to converge gradually. The strain energy density under the N^{th} cycle can be calculated as $W(\lambda_{max}, N) = \int_1^{\lambda_{max}} P d\lambda$ from the P versus λ curve of unnotched samples (Fig. S3B). Then, the cyclic tensile test with the same λ_{max} was applied to the notched sample. The digital microscope (AM4815ZT, Dino-Lite; resolution, 20 mm/pixel) was used to record the crack length $l(N)$ and crack growth rate dl/dN on the notched sample over the N^{th} cycles. The applied energy release rate G in the notched sample with the maximum applied stretch of λ_{max} can be calculated as $G(\lambda_{max}, N) = 2k(\lambda_{max}) \cdot l(N) \cdot W(\lambda_{max}, N)$, where $k = 3/\sqrt{\lambda_{max}}$[43]. For each material, the curve of crack growth rate dl/dN versus the applied energy release rate G can be acquired by doing tests with different λ_{max}. The applied energy release rate G when the crack growth rate begins to increase significantly can be regarded as the fatigue threshold G_c (Fig. S3C). Note that the resolution of dl/dN is 0.002 μm/cycle because the resolution of the digital camera is about 0.02 mm (20 μm/pixel). Then the crack propagation area rate can be calculated as $dc/dN = dl/dN \cdot t$, where t is the thickness of sample.

Characterization of abrasion emissions

To characterize abrasion emissions, a motor-controlled rotating wheel (diameter 20 cm) with organic samples firmly bonded to the wheel by a superglue is housed in a closed chamber. The chamber was made of acrylic plastics (McMaster-Carr). The rotating speed of the wheel is 300 rpm that is corresponding to 5 Hz. Sandpaper (15 mm by 15 mm) with different grit sizes was glued on a rigid plastic plate and forced to contact the organic samples with normal forces controlled by a force gauge (LANDTEK, FM-204-100 K). A particle counter (TENMA, 72–10190) was fixed at 20 cm from the abrasion region to record the concentration of the emitted particles with different sizes (0.3 μm, 1 μm, 2.5 μm, 5 μm, 10 μm). The particle counter (TENMA, 72-10190) is an optical particle sizer with 6 channels: 0.3 μm, 0.5 μm, 1.0 μm, 2.5 μm, 5.0 μm, and 10 μm, whose counting efficiency is 50% at 0.3 μm and 100% for particles larger than 0.45 μm. Coincidence loss is 5%, 2,000,000 particles per ft^3. The concentration of PM10 is calculated by summing up the concentration of particles with sizes of 0.3 μm to 10 μm. A microscope slide attached with double-sided carbon tape was fixed next to the particle counter to collect the emitted particles for the purpose of imaging. The microscope images were taken by an optical microscope (Nikon ECLIPSE LV100ND).

Characterization of sandpaper grits

Grits of each sandpaper (type 40, 60, 80, 120, 150, 180, 220 from 3 M company) were imaged by a scanning electron microscope (Nova NanoSEM 450) and processed with ImageJ software. To obtain the grit size distribution for each sandpaper, 100 grits on the sandpaper were randomly picked to measure the grit diameter. The average diameter and the standard deviation were calculated by assuming the particle size distribution follows the normal distribution and fitting the statistical data.

Measurement of the coefficient of friction of the sandpapers

To measure the kinetic friction of each material on the sandpaper, we carried out sliding friction tests under the ASTM D1894 standard with a mechanical tester (Instron, Model 5942).

Data availability

All data needed to evaluate the conclusions in the paper are present in the paper and/or the Supplementary Materials. Additional data related to this paper may be requested from the corresponding author.

Received: 10 November 2023; Accepted: 24 September 2024
Published online: 10 October 2024

References

1. Penkała, M., Ogrodnik, P. & Rogula-Kozłowska, W. Particulate matter from the road surface abrasion as a problem of non-exhaust emission control. *Environments* **5**(1), 9 (2018).
2. Thorpe, A. & Harrison, R. M. Sources and properties of non-exhaust particulate matter from road traffic: A review. *Sci. Total Environ.* **400**(1), 270–282 (2008).

3. Pant, P. & Harrison, R. M. Estimation of the contribution of road traffic emissions to particulate matter concentrations from field measurements: A review. *Atmos. Environ.* **77**, 78–97 (2013).
4. Maricq, M. M. Engine, aftertreatment, fuel quality and non-tailpipe achievements to lower gasoline vehicle PM emissions: Literature review and future prospects. *Sci. Total Environ.* **866**, 161225 (2022).
5. Ntziachristos, L. & Boulter, P. Road vehicle tyre and brake wear. Road surface wear. *Joint EMEP/CORINAIR emission inventory guidebook*:B770-771 (2003).
6. Lewis, A., Moller, S.J., & Carslaw, D, Non-exhaust emissions from road traffic (2019).
7. Sommer, F. *et al.* Tire abrasion as a major source of microplastics in the environment. *Aerosol Air Qual. Res.* **18**(8), 2014–2028 (2018).
8. Kole, P. J., Löhr, A. J., Van Belleghem, F. G. & Ragas, A. M. Wear and tear of tyres: a stealthy source of microplastics in the environment. *Int. J. Environ. Res. Public Health* **14**(10), 1265 (2017).
9. Knight, L. J., Parker-Jurd, F. N. F., Al-Sid-Cheikh, M. & Thompson, R. C. Tyre wear particles: an abundant yet widely unreported microplastic?. *Environ. Sci. Pollut. Res.* **27**(15), 18345–18354 (2020).
10. Wagner, S. *et al.* Tire wear particles in the aquatic environment—A review on generation, analysis, occurrence, fate and effects. *Water Res.* **139**, 83–100 (2018).
11. Evangeliou, N. *et al.* Atmospheric transport is a major pathway of microplastics to remote regions. *Nat. Commun.* **11**(1), 3381 (2020).
12. Gerlofs-Nijland, M. E. *et al.* Inhalation toxicity profiles of particulate matter: a comparison between brake wear with other sources of emission. *Inhal. Toxicol.* **31**(3), 89–98 (2019).
13. Jalali Farahani, V., Altuwayjiri, A., Taghvaee, S. & Sioutas, C. Tailpipe and nontailpipe emission factors and source contributions of PM10 on major freeways in the Los Angeles basin. *Environ. Sci. Technol.* **56**(11), 7029–7039 (2022).
14. Pant, P. & Harrison, R. H. Estimation of the contribution of road traffic emissions to particulate matter concentrations from field measurements: A review. *Atmos. Environ.* **77**, 78–97 (2013).
15. Chen, Q. *et al.* An emerging role of microplastics in the etiology of lung ground glass nodules. *Environ. Sci. Eur.* **34**(1), 25 (2022).
16. Huang, S. *et al.* Detection and analysis of microplastics in human sputum. *Environ. Sci. Technol.* **56**(4), 2476–2486 (2022).
17. Jo, E.-J. *et al.* Effects of particulate matter on respiratory disease and the impact of meteorological factors in Busan, Korea. *Respir. Med.* **124**, 79–87 (2017).
18. Lee, B.-J., Kim, B. & Lee, K. Air pollution exposure and cardiovascular disease. *Toxicol. Res.* **30**(2), 71–75 (2014).
19. Li, J., Li, W. X., Bai, C. & Song, Y. Particulate matter-induced epigenetic changes and lung cancer. *Clin. Respir. J* **11**(5), 539–546 (2017).
20. Rahman, A., Sarkar, A., Yadav, O. P., Achari, G. & Slobodnik, J. Potential human health risks due to environmental exposure to nano-and microplastics and knowledge gaps: A scoping review. *Sci. Total Environ.* **757**, 143872 (2021).
21. Yang, Y. *et al.* Detection of various microplastics in patients undergoing cardiac surgery. *Environ. Sci. Technol.* **57**(30), 10911–10918 (2023).
22. Buckeridge, D. L. *et al.* Effect of motor vehicle emissions on respiratory health in an urban area. *Environ. Health Perspect.* **110**(3), 293–300 (2002).
23. Fan, Z. *et al.* Acute short-term exposures to PM2.5 generated by vehicular emissions and cardiopulmonary effects in older adults. *Epidemiology* **17**(6), S213–S214 (2006).
24. Pollution HEIPotHEoT-RA. Traffic-related air pollution: a critical review of the literature on emissions, exposure, and health effects (2010).
25. Masiol, M. *et al.* Carcinogenic and mutagenic risk associated to airborne particle-phase polycyclic aromatic hydrocarbons: A source apportionment. *Atmos. Environ.* **60**, 375–382 (2012).
26. Cadle, S. & Williams, R. Gas and particle emissions from automobile tires in laboratory and field studies. *Rubber Chem. Technol.* **52**(1), 146–158 (1979).
27. Tonegawa, Y. & Sasaki, S. Development of tire-wear particle emission measurements for passenger vehicles. *Emiss. Control Sci. Technol.* **7**(1), 56–62 (2021).
28. Harrison, R. M., Jones, A. M., Gietl, J., Yin, J. & Green, D. C. Estimation of the contributions of brake dust, tire wear, and resuspension to nonexhaust traffic particles derived from atmospheric measurements. *Environ. Sci. Technol.* **46**(12), 6523–6529 (2012).
29. Panko, J., Kreider, M. & Unice, K. Chapter 7—Review of tire wear emissions: A review of tire emission measurement studies: Identification of gaps and future needs. In *Non-Exhaust Emissions* (ed. Amato, F.) 147–160 (Academic Press, 2018).
30. Archard, J. Contact and rubbing of flat surfaces. *J. Appl. Phys.* **24**(8), 981–988 (1953).
31. Suh, N. P. The delamination theory of wear. *Wear* **25**(1), 111–124 (1973).
32. Champ, D. H., Southern, E. & Thomas, A. G. Fracture mechanics applied to rubber abrasion. In *Advances in Polymer Friction and Wear* (ed. Lee, L.-H.) 133–144 (Springer US, 1974).
33. Akono, A.-T. & Ulm, F.-J. Scratch test model for the determination of fracture toughness. *Eng. Fract. Mech.* **78**(2), 334–342 (2011).
34. Akono, A.-T., Reis, P. M. & Ulm, F.-J. Scratching as a fracture process: From butter to steel. *Phys. Rev. Lett.* **106**(20), 204302 (2011).
35. Akono, A.-T. & Ulm, F.-J. Fracture scaling relations for scratch tests of axisymmetric shape. *J. Mech. Phys. Solids* **60**(3), 379–390 (2012).
36. Akono, A.-T. & Ulm, F.-J. An improved technique for characterizing the fracture toughness via scratch test experiments. *Wear* **313**(1–2), 117–124 (2014).
37. Paris, P. C. A rational analytic theory of fatigue. *Trends Eng.* **13**, 9–14 (1961).
38. Gent, A., Lindley, P. & Thomas, A. Cut growth and fatigue of rubbers. I. The relationship between cut growth and fatigue. *J. Appl. Polym. Sci.* **8**(1), 455–466 (1964).
39. Lake, G. & Lindley, P. Cut growth and fatigue of rubbers. II. Experiments on a noncrystallizing rubber. *J. Appl. Polym. Sci.* **8**(2), 707–721 (1964).
40. Johnson, K. L. & Johnson, K. L. *Contact Mechanics* (Cambridge University Press, 1987).
41. Prisacariu, C. *Polyurethane Elastomers: From Morphology to Mechanical Aspects* (Springer Science & Business Media, 2011).
42. Kinloch, A. J. *Fracture Behaviour of Polymers* (Springer Science & Business Media, 2013).
43. Lin, S. *et al.* Anti-fatigue-fracture hydrogels. *Sci. adv.* **5**(1), eaau8528 (2019).
44. Kipscholl, R. & Stoček, R. Degradation of tires during intended usage. In *Degradation of Elastomers in Practice, Experiments and Modeling* (eds Heinrich, G. et al.) 185–207 (Springer, 2022).
45. Chang, K., Jia, H. & Gu, S.-Y. A transparent, highly stretchable, self-healing polyurethane based on disulfide bonds. *Eur. Polym. J.* **112**, 822–831 (2019).
46. Motokucho, S., Furukawa, M., Kawashima, M., Kojio, K. & Yoshinaga, K. Physical properties of poly (tetrahydrofuran)-block-poly (2-ethyl-2-oxazoline) triblock copolymer. *Polym. J.* **45**(11), 1115 (2013).

Acknowledgements

Q.W. acknowledges the funding support from the National Science Foundation (CMMI-1943598, CMMI-2229228, and DBI-2222206) and the Office of Naval Research (N00014-22-1-2019).

Author contributions

K.L., K.Y., C.S., and Q.W. designed the research. K.L. and K.Y. carried out experiments with the technical support of Y.Z. and H.D.. K.L. and Q.W. developed the theory. K.L., K.Y., C.S., and Q.W. interpreted the results and wrote the manuscript. All authors contributed to revising the manuscript. Q.W. and C.S. supervised the research.

Funding

The funding was supported by National Science Foundation, 1943598, Office of Naval Research, N00014-22-1-2019.

Declarations

Competing interests

The authors declare no competing interests.

Additional information

Supplementary Information The online version contains supplementary material available at https://doi.org/10.1038/s41598-024-74137-6.

Correspondence and requests for materials should be addressed to C.S. or Q.W.

Reprints and permissions information is available at www.nature.com/reprints.

Publisher's note Springer Nature remains neutral with regard to jurisdictional claims in published maps and institutional affiliations.